GPS Solutions (2024) 28:23
https://doi.org/10.1007/s10291-023-01564-9

RESEARCH

Co-seismic ionospheric disturbances characteristics in different azimuths following the 2022 Mexico earthquake from GNSS observations

Linlin Li[1,2] · Shuanggen Jin[1,3] · Yi Chai[1,2]

Received: 29 May 2023 / Accepted: 9 October 2023

Abstract
Co-seismic ionospheric disturbances (CIDs) can help understand the coupled dynamics of earthquake-atmospheric coupling geophysical processes. On September 19, 2022, an earthquake occurred at UTC = 18:05:08 near the Pacific Coast of Mexico as the result of shallow thrust faulting with magnitude of 7.6 and depth of around 26.9 km. The epicenter of the earthquake is located at (18.455°N, 102.956°W). In this study, observation data from the global navigation satellite system (GNSS) are used to identify CIDs about 12 min after the earthquake occurred. The significant CIDs signals are observed with extending outward from the epicenter. The CID characteristics like amplitude, frequency, and waveform are also investigated and discussed. The waveform is a standard and inverse *N*-type, suggesting a connection to plate movement and geomagnetic field. In addition, the center frequency is within the range of acoustic wave frequency from 2 to 4 mHz. The propagation speed is approximately 0.81 km/s for PRN G18, 1.01 km/s for G23, and 1.16 km/s in the east and 1.44 km/s in the west for G32 between 18:00 and 19:00. For R21, the propagation speed is close to 1.06 km/s. It demonstrates that the main source of the CIDs is the acoustic wave. Also, it is discovered that the CID propagation velocity varies significantly depending on the azimuth. At the direction closed to the strike angle (287°), the maximum propagation speed is found. The rupture mainly occurred in the western region, and the rupture velocity is larger in the western region, which might cause the quicker CID in this direction.

Keywords GNSS · Earthquake · Ionosphere · CIDs

Introduction

Earthquakes are normally generated by the quick release of energy from the Earth's crust, which have a tremendous destructive effect on the Earth's surface and can result in massive human losses. Thus, it is of vital importance to monitor and investigate the earthquake. When an earthquake occurs, the generated power not only harms the Earth's surface, but also spreads to the ionosphere, leading to a change in ionospheric electron density. As a result, ionospheric anomaly induced by earthquakes can be detected.

Satellite observation provides worldwide, short-cycle, high efficiency, and the high-quality data to monitor earthquakes that effectively compensate the drawbacks from conventional observation methods. Global positioning system (GPS) provides a powerful and easy way for remoting sensing of the ionosphere and monitor earthquake ionospheric disturbances (Calais and Minster 1995). In comparison to conventional observation methods, multi-GNSS systems and dense GNSS observation networks can cover and monitor the whole ionosphere. GNSS observations deliver high spatial and temporal resolution ionospheric total electron content (TEC) data, which have impactful scientific and practical importance for ionospheric delay correction and space environment monitoring (Heise et al. 2002). Geodesy, space physics, and other fields have paid close attention to GNSS ionosphere study and development (Astafyeva et al. 2014a, b; Cahyadi and Heki 2015; Zakharov and Gorchakov 2017; Virgile et al. 2017).

✉ Shuanggen Jin
sgjin@shao.ac.cn

[1] Shanghai Astronomical Observatory, Chinese Academy of Sciences, Shanghai 200030, China

[2] School of Astronomy and Space Science, University of Chinese Academy of Sciences, Beijing 100049, China

[3] School of Surveying and Land Information Engineering, Henan Polytechnic University, Jiaozuo 454003, China

Published online: 06 November 2023

Calais and Minster (1995) utilized GPS observation data to detect the obvious ionospheric disruption around the epicenter of the Northridge earthquake. According to the disturbance period and velocity, the atmospheric acoustic-gravity wave was considered to be the main source of this disturbance. The ionospheric disturbance in the far field has a faster propagation speed, which is equivalent to the speed of seismic Rayleigh waves (Ducic et al. 2003). The far-field ionospheric disturbance propagates in the same mode as seismic Rayleigh waves as it is regarded to be a secondary acoustic disturbance triggered by these waves in the crust of the Earth. Later, Artru et al. (2004) discovered that the propagation velocity of the ionospheric disturbance was between 150 and 250 m/s using GPS observation data. In 2011, a Mw = 9.0 earthquake occurred in Tohoku, Japan. With the dense GNSS network around, cases studies showed that 2 h after the earthquake, the ionospheric disturbances were driven by gravity waves moving at several hundred meters per second, acoustic waves traveling at around 1 km/s second, and seismic Rayleigh waves transiting at about 2–4 km/s (Tsugawa et al. 2011; Liu et al. 2011; Jin et al. 2015). Till now, many studies have shown that CIDs have many differences in propagation speed, frequency, direction and amplitude (Afraimovich et al. 2001; Heki and Ping 2005; Astafyeva et al. 2009; Chai and Jin 2021). On the whole, there are three different categories of seismic ionospheric disturbance: direct acoustic wave from the earthquake area, gravity wave propagating obliquely upward from the focal area, and secondary acoustic wave excited in areas away from the epicenter by Rayleigh surface wave.

Nonetheless, there are still uncertain issues and difficulties in the study of CIDs. For instance, the relationship between detailed propagation characteristics of CIDs and focal surface deformation (Astafyeva et al. 2013) is still not clear. Also, the ground-based GNSS network distribution is uneven without all-azimuth coverage near the epicenter. For the quantitative investigation, the coupling mechanism of earthquake-atmosphere–ionosphere still needs to be confirmed. The propagation of CIDs is affected by seismic parameters, geomagnetic field, and atmosphere (Heki and Ping 2005; Astafyeva et al. 2009; Heki et al. 2006; Rolland et al. 2011, 2013; Afraimovich et al. 2001; Bagiya et al. 2019). In addition, GNSS detection of CIDs is also affected by the geometric position of the GNSS line of sight signal (Afraimovich et al. 2001; Astafyeva et al. 2014a, b). Therefore, the investigation on different kinds of earthquakes is important to clarify CID characteristics and the coupling mechanism of earthquake-atmosphere–ionosphere, particularly full-azimuth satellite coverage for the Mexico earthquake on September 19, 2022. However, the study of CIDs on the 2022 Mexico earthquake is still very limited and in particularly CID characteristics in different azimuths are unknown in the term of speed, amplitude, frequency, and waveform.

In this study, the seismic ionospheric disturbances characteristics are estimated and analyzed following the 2022 Mexico earthquake from GNSS observations. Some coupling mechanism is also discussed. In the following sections, data and methods are introduced, results and analysis are presented as well as discussion, and finally summary is given.

Data and methods

This section provides some details about the 2022 Mexico earthquake and presents the datasets and methods in this study. An overview includes the Mexico earthquakes occurred in history and the details of this event like surface rupture and so on in the next part. The datasets and method in this study are described.

The 2022 Mexico earthquake and GNSS data

On September 19, 2022, a Mw = 7.6 earthquake (18.455°N, 102.956°W) occurred near the Pacific Coast of Mexico at UTC = 18:05:08 with a focal depth of about 26.9 km according to U.S. Geological Survey National Earthquake Information Center (USGS-NEIC). Tectonic strain accumulation along the Mexican subduction zone is produced by the Rivera and Cocos plates underthrusting the North American plate at from 2.5 to 7.0 cm per year (DeMets et al. 2010). Before September 19, 2022, there were several earthquakes occurred in this region, such as June 3, 1932 Jalisco earthquake (Ms = 8.2) (Singh et al. 1985), the Colima-Jalisco megathrust earthquake (Mw = 8.0) on October 9, 1995 (Mendoza and Hartzell 1999; Ortiz et al. 1998), a megathrust rupture earthquake on January 30, 1973 (Mw = 7.6) (Reyes and Brune 1979; Santoyo et al. 2006), an earthquake on September 19, 1985 (Mw = 8.1) (Mendoza and Hartzell 1989), the Tecoman earthquake (Mw = 7.6) on January 22, 2003 (Yagi et al. 2004), and other smaller earthquakes. As shown in Fig. 1, the W-phase solution suggests a predominantly shallowly dipping thrust mechanism with strike $\Phi = 287°$, dip $\delta = 18°$, and rake $\lambda = 86°$. Slip is concentrated offshore and below the coast at depths from 10 to 30 km with a peak value of ~2.9 m, and there is no detected co-seismic slip near the trench. The total seismic moment is 3.1 × 10^20 N·m (Mw 7.6), and 72% of which is concentrated in the first 30 s. Most aftershocks are distributed in an up-dip area of the mainshock with small co-seismic slip, suggesting near-complete strain release in the large-slip patch (Liu et al. 2023).

The ionospheric disturbance may be influenced by space weather. To exclude the factor, the space weather indexes from September 18–20 are shown in Fig. 2 from space physics data facility (SPDF, https://cdaweb.gsfc.nasa.gov/). The Dst was more than − 40 nT, and Kp was less than 5, which means it

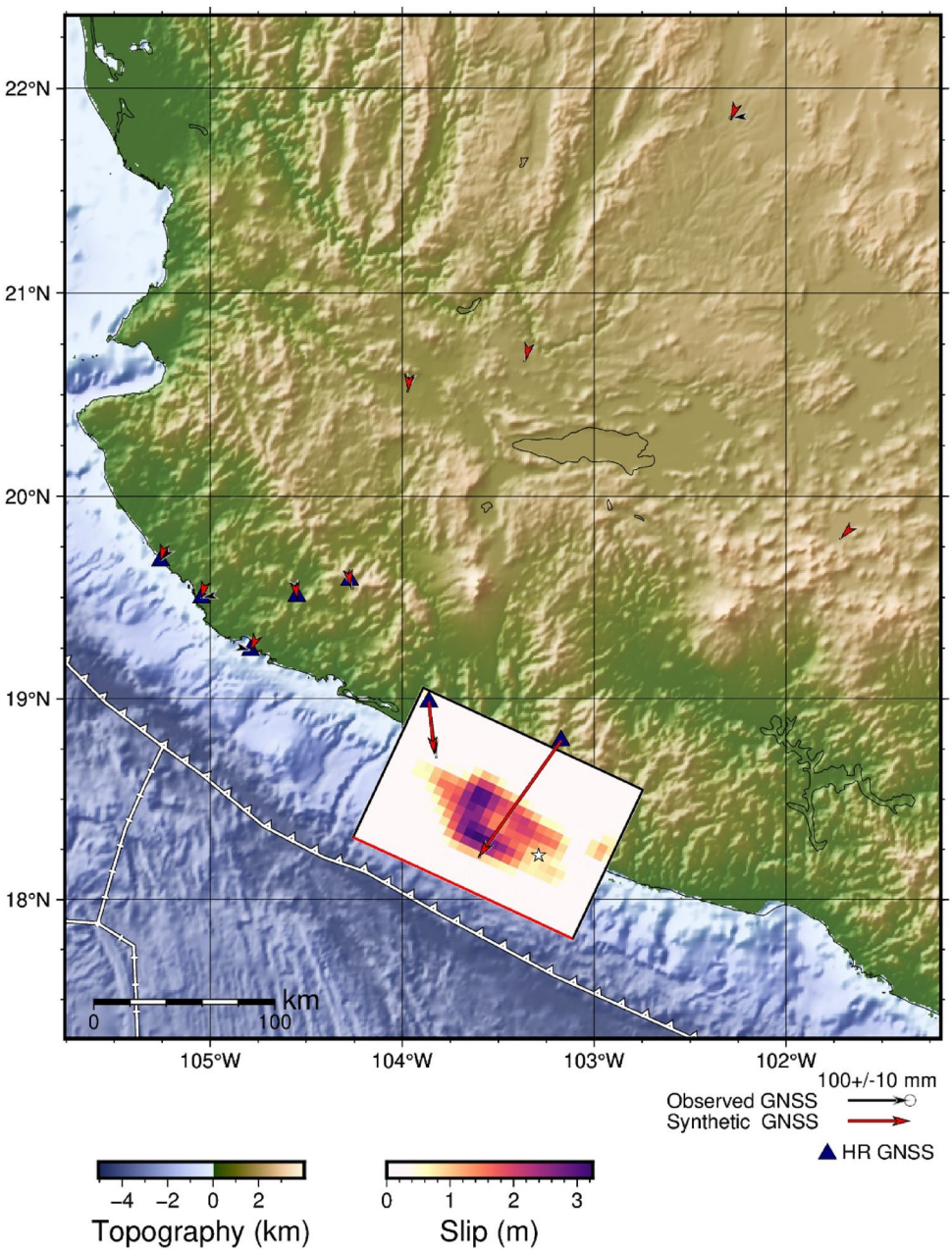

Fig. 1 Surface projection of the slip distribution superimposed on GEBCO bathymetry (https://earthquake.usgs.gov/earthquakes/eventpage/us7000i9bw/finite-fault). Thick white lines indicate major plate boundaries (Bird 2003)

was a geomagnetic calm day on September 19, 2022. Here, the GNSS observation data were downloaded from UNAVCO (https://www.unavco.org/data/), which are shown in Fig. 3.

Method of CID estimation

To obtain the ionospheric disturbances during the earthquakes, the TEC is calculated from the dual-frequency GNSS observation by the following equations (Brunini and Azpilicueta 2009; Jin et al. 2017):

$$\mathrm{STEC} = \frac{f1^2 f2^2}{40.3\left(f1^2 - f2^2\right)} \left(L1 - L2 + \lambda 1(N1 + b1) - \lambda 2(N2 + b2) + \varepsilon_L\right) \quad (1)$$

$$\mathrm{STEC} = \frac{f1^2 f2^2}{40.3\left(f1^2 - f2^2\right)} \left(P1 - P2 - (d1 - d2) + \varepsilon_P\right) \quad (2)$$

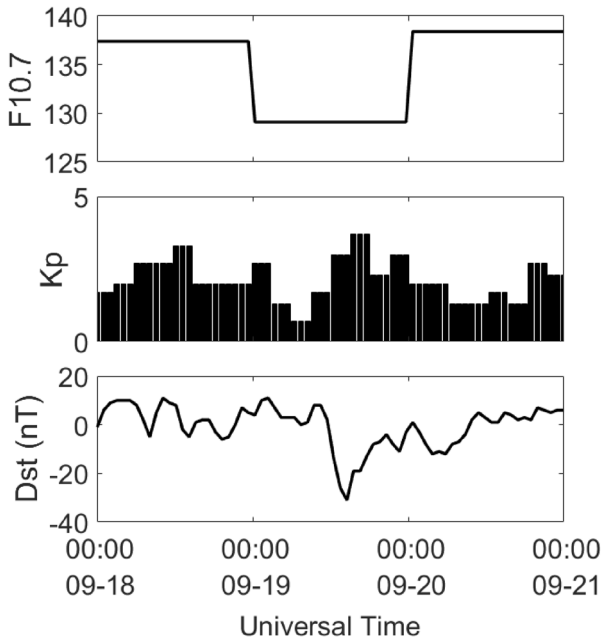

Fig. 2 Space weather situation on September 19, 2022 with F10.7 (top panel), Kp index (middle panel) and Dst index (bottom panel)

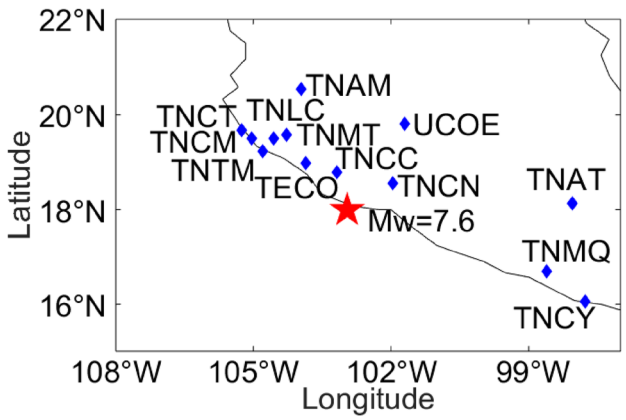

Fig. 3 GNSS Stations and the earthquake location. The blue diamonds represent the GNSS stations, and the red star represents the earthquake epicenter

where STEC is the slant total electron content in TECU (1 TECU = 1e16 m^{-2}), L1 and L2 are the GPS carrier phase in different frequencies, $\lambda 1$ and $\lambda 2$ are the GPS signal wavelength in different frequencies, N is the ambiguity, b is the instrument biases for carrier phase, $d1$ and $d2$ are the differential code biases, and ε is the residual.

With the mapping function below, the STEC is transferred to vertical TEC (VTEC) (Jin et al. 2012; Gao et al. 2020):

$$F(\varepsilon) = \frac{STEC}{VTEC} = \frac{1}{\cos\alpha} = \frac{1}{\sqrt{1-\left(\frac{R_{earth}}{R_{earth}+H_{ion}}\cos(\varepsilon)\right)^2}} \quad (3)$$

where R_{earth} is the earth radius, H_{ion} is the height of single shell ionosphere, α is the zenith distance of the satellite relative to the sub-ionospheric piercing point (SIP), and ε is the altitude angle of the satellite relative to the receiver. In this case, the H_{ion} is assumed as 350 km of average maximum ionospheric electron density height. In order to obtain the GNSS-TEC residual time series, which represents the relative change in VTEC, a fourth-order Butterworth filter is utilized. Above the ionospheric height, the acoustic cut-off frequency is around 2 mHz (Chai et al., 2020). The Nyquist frequency for GNSS observation is greater than 8 mHz following the Nyquist sampling theory, because the GNSS sampling interval is 15 s. Therefore, the 2–5 mHz passband frequency filtering is used to extract the co-seismic ionospheric disturbance (CID) in this case.

Results and analysis

In this section, we first estimated and analyzed the CID at several stations following the 2022 Mexico Earthquake and conducted spectral analysis. The propagation details of different satellites and station combinations are also discussed.

CIDs following the 2022 Mexico earthquake

The CIDs following the 2022 Mexico earthquake were detected and displayed in Fig. 4. Several satellite and station pairings are made. The filtered TEC range is different among different combinations, and the time period is from 18:00 to 18:30. For the same satellite (subgraphs in the same row in Fig. 4), TEC from station TNLC is a little larger than station TNTM. Filtered TEC from satellite G32 is smaller than G18, G23 and R21, which is nearly one half numerically. For the same station like TNLC, the range of filtered TEC is about − 0.064 TECU to 0.090 TECU from G18. From G23, it is from − 0.071 TECU to 0.060 TECU. The filtered TEC obtained from G32 is from − 0.029 TECU to 0.040 TECU. As for the R21, it is from − 0.067 TECU to 0.079 TECU. Typical *N*-type signals are found with the combination of stations and G23 in Fig. 4c and d, while inverted *N*-type signals are found with the combination of stations and G18, G23 and R21.

After applying a short-time Fourier transform, Fig. 5 shows the spectrograms of the TEC time series that have been filtered from the various combinations of stations and

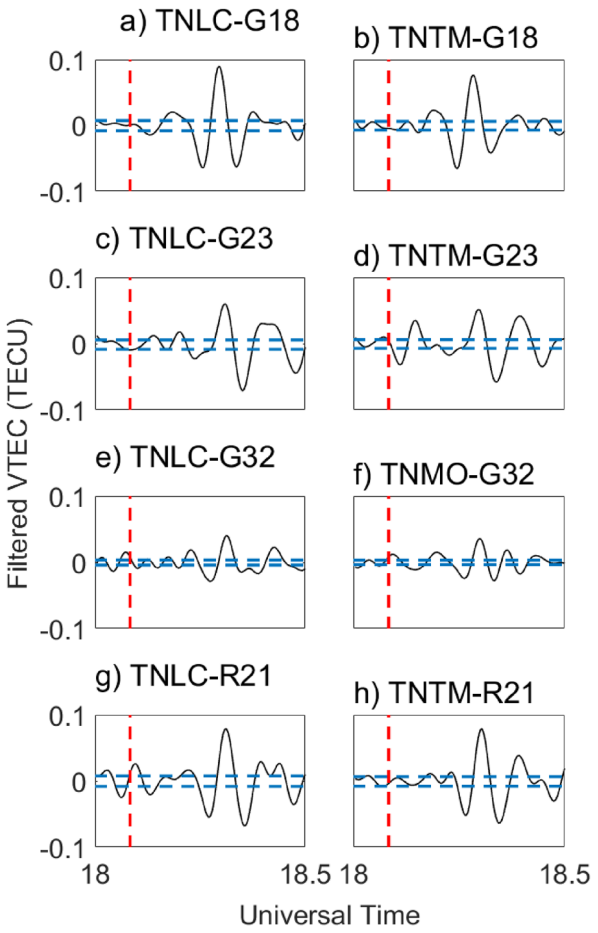

Fig. 4 Filtered TEC time series following the 2022 Mexico earthquake from the combination of station and satellites during 18:00–18:30

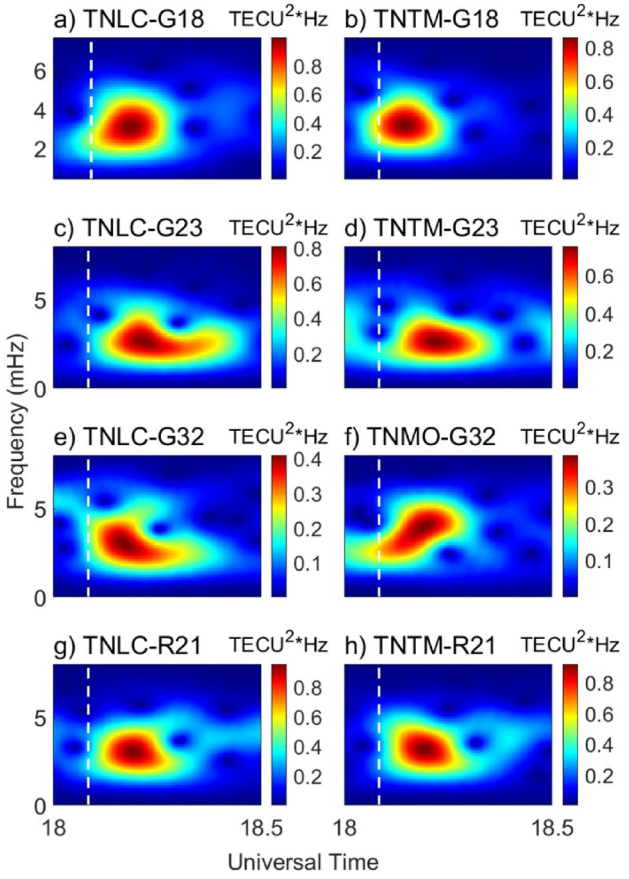

Fig. 5 Spectrograms of filtered TEC from the combination of station and satellites during the 18:00–18:30

satellites. Although the combinations are various, the central frequencies are similar, which are approximately 3 mHZ during 18:00–18:30.

In Fig. 6, the SIP tracks of G18, G23, G32 and R21 are shown during 18:06–18:30. The range of color bar is from − 0.1 TECU to 0.1 TECU. The time interval is 6 min. It demonstrates that the obvious CIDs are appeared in the northwest region. For the northwest region, the SIP tracks are less. Thus, it is hard to get details in this region. With Figs. 4 and 6, the CIDs appear 10 min after the earthquake and disappear 20 min after the earthquake.

Propagation velocity

The CID propagation velocity is estimated and analyzed in this section. G18, G23, G32 and R21 are chosen to calculated the CID speed in different directions, and the results are shown in Figs. 7, 8, 9, 10 and 11 (The G32 is divided into two figures because of the azimuth). The SIP tracks can be seen in Figs. 7, 8, 9, 10 and 11 on the right top panels. The velocities are 0.81 km/s, 1.01 km/s, 1.16 km/s, 1.44 km/s and 1.06 km/s, respectively. The speeds are the same as the acoustic wave velocity. The CIDs with such kind of speeds might be caused by the rupture and deformation of the epicenter plate. However, the velocity is a little different from each other especially 1.44 km/s. CID speeds in different azimuth directions are summarized in Fig. 12. It is demonstrated that maximum velocity appears at about 283°, which is close to the strike (287°).

Among Figs. 7, 8, 9, 10 and 11, it is found that the filtered TEC is more obvious in near region and the amplitude is decreased with the increase in the distance from the epicenter. Moreover, the velocity steadily is decreased with the time passing by, and the ionosphere is calm around 20 min after the earthquake.

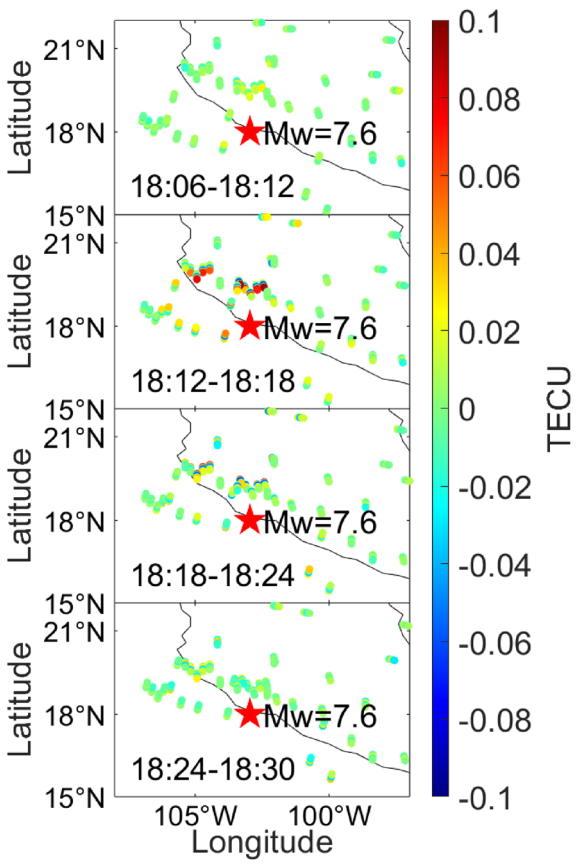

Fig. 6 Filtered TEC distribution maps extracted from GNSS observation data during 18:06–18:30 on September 19, 2022, and the time interval is 6 min. The red star is the earthquake epicenter. The dots present the SIPs, and the color bar is the variation range of filtered TEC

Discussion

The CIDs following the 2022 Mexico earthquake were extracted from GNSS observation data for G18, G23, G32 and R21. They were detected within about 12 min of the shock and vanished after about 20 min. The CIDs appeared mainly in the north of the region and then, propagated away from the epicenter. Fault dislocation of an earthquake causes vertical movement of the earth surface and excites atmospheric waves. They propagate upward and often disturb the ionosphere. Its first phase starts about 12 min after an earthquake, when acoustic waves reach the ionospheric F region. Such CIDs usually occur as transient disturbances with periods of several minutes, but may last for hours after very large earthquakes. On the other hand, physical mechanisms responsible for ionospheric changes immediately before large earthquakes remain elusive.

For the same station like TNLC, the range of filtered TEC is about − 0.064 TECU to 0.090 TECU from G18. For G23, it is from − 0.071 TECU to 0.060 TECU. The filtered TEC obtained from G32 is from − 0.029 TECU to 0.040 TECU. As for the R21, it is from − 0.067 TECU to 0.079 TECU. The range is different from each other and the station with G32 is especially small, which is near half of the values from other combinations. The mean elevation angle and distance of the different satellites with TNLC are calculated, which are shown is Fig. 12. The angle between the wave front and the line of sight affects the visible disturbance's amplitude, which increases if the two are parallel at ionospheric height. To the similar elevation angle like G18 and G32, the distance of G32 is larger. These kinds of geometry effects have been noticed in the previous studies (Heki et al. 2006; Chai et al. 2020).

The waveform can be divided to typical "*N*-type" and inverted *N*-type waves (Heki and Ping 2005; Afraimovich et al. 2001). The final wave form is affected by factors such as the geometry of line of sight, disturbance wavefront, geomagnetic field and filtering method. Furthermore, it is known Tsemplen theorem states that a rarefaction shock wave cannot exist as a discontinuity. According to the observation findings, the reverse *N*-type wave's amplitude is smaller than that of the normal wave, which may reflect its inherent instability. Thus, the effect of the geomagnetic field, geometric factors and filtration parameters may be responsible for the appearance of the inverted N wave.

From Fig. 5, the CID center frequency is around 3.3 mHz. Due to the atmospheric filtering effect (Blanc 1985), only frequency components with durations of a few minutes can pass to the ionosphere without substantial attenuation. The original atmospheric waves would have a broad range of frequency spectra in the case of co-seismic ionospheric disturbances, but those close to the acoustic cut-off (periods 4–5 min) would stay at the ionospheric height.

In addition, the CID propagation speed shows some intriguing characteristics, although seismic ionospheric effects ought to be isotropic based on earlier studies. The velocity varies significantly with various combinations. The velocity is 0.81 km/s, 1.01 km/s, 1.15 km/s, 1.44 km/s, and 1.06 km/s, respectively, as shown in Figs. 7, 8, 9, 10 and 11. According to the analysis in Fig. 13, the CID spreads more quickly in the direction of azimuth around 283°. From beach ball in the same Figure, the strike is 287°. From Fig. 1, the rupture mainly occurred in the western region. The rupture velocity in the western region is about 0.10–0.15 m/s from

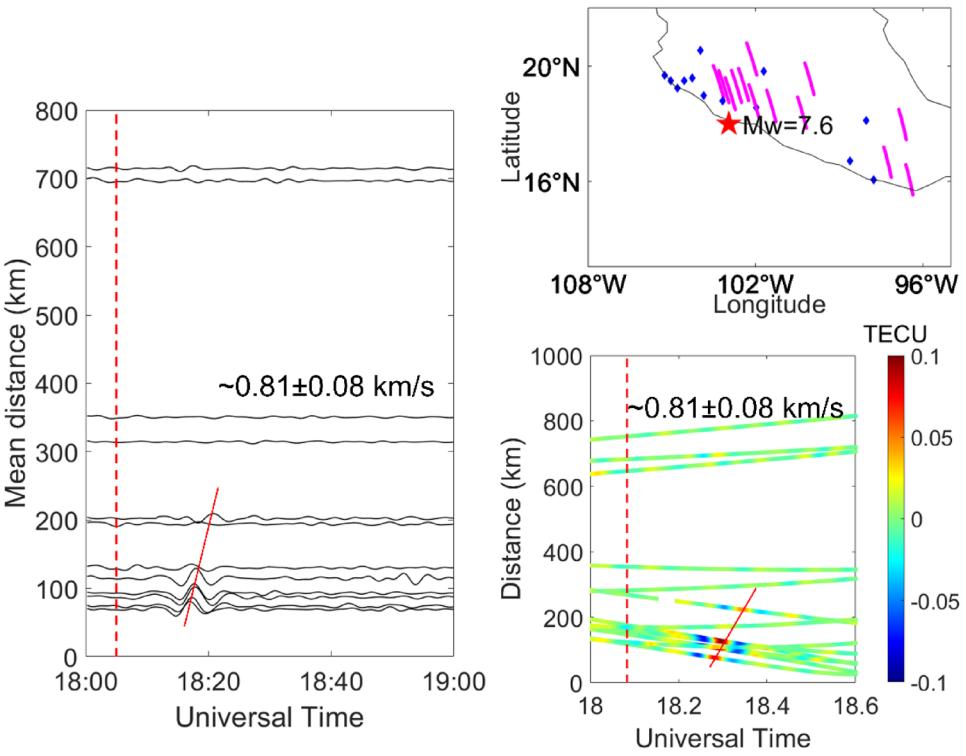

Fig. 7 CIDs from GNSS stations for G18 during 18:00–19:00 with the TEC time series (left panel), SIPs track (top right panel) and the travel time diagram (bottom right panel)

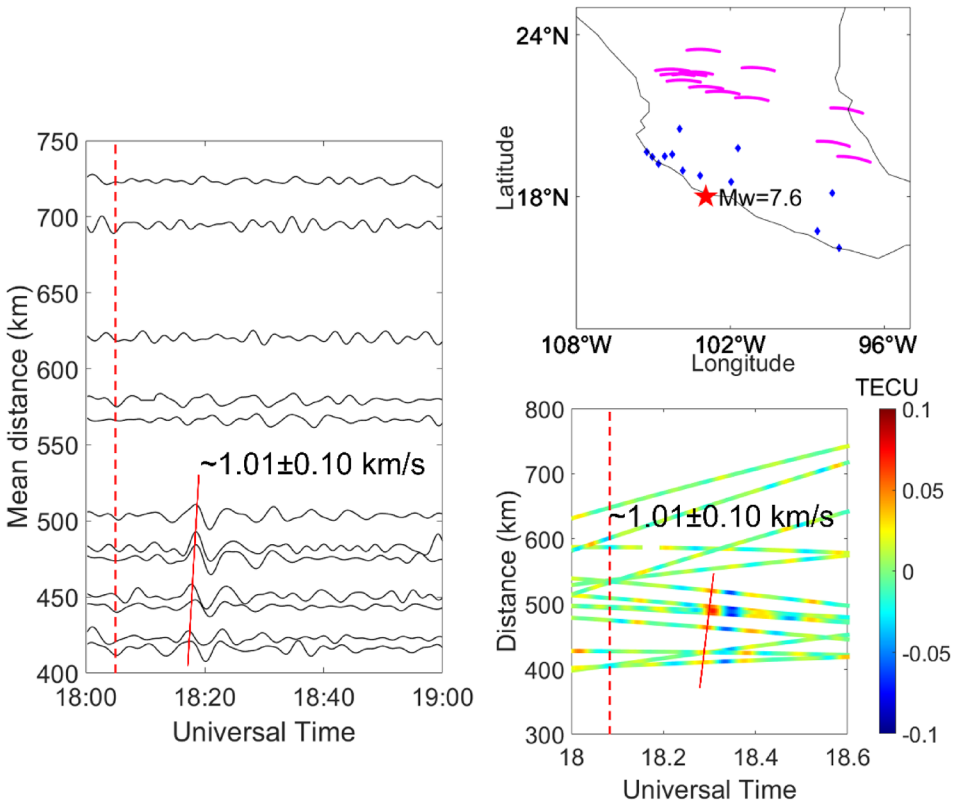

Fig. 8 CIDs from GNSS stations for G23 during 18:00–19:00 with TEC time series (left panel), SIPs track (top right panel) and the travel time diagram (bottom right panel)

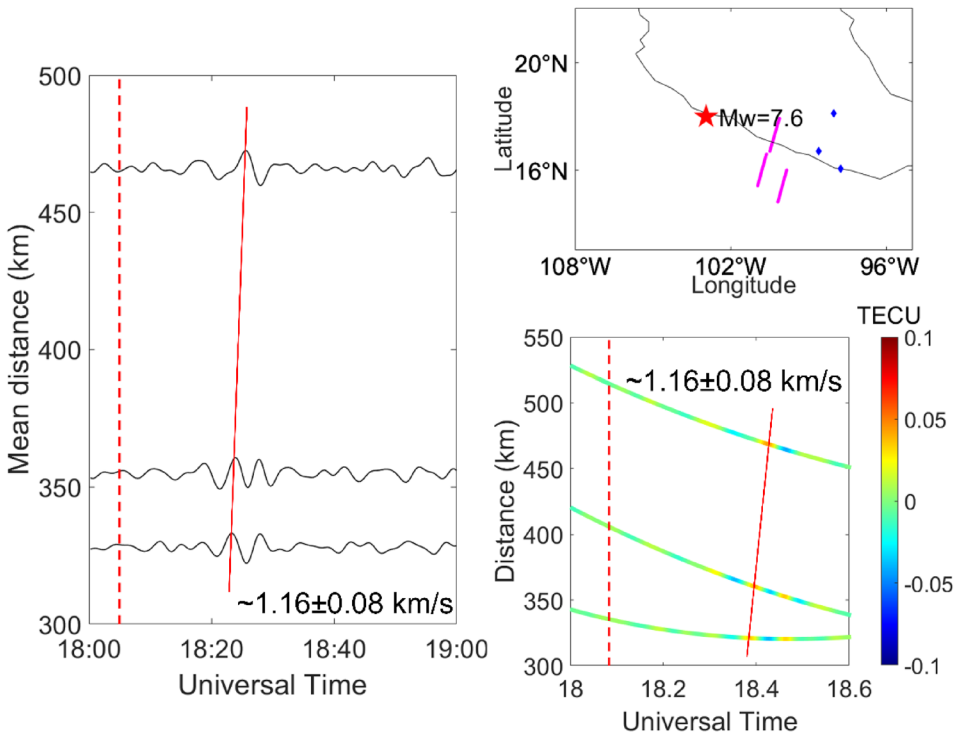

Fig. 9 CIDs from GNSS stations for G32 during 18:00–19:00 with TEC time series (left panel), SIPs track (top right panel) and the travel time diagram (bottom right panel)

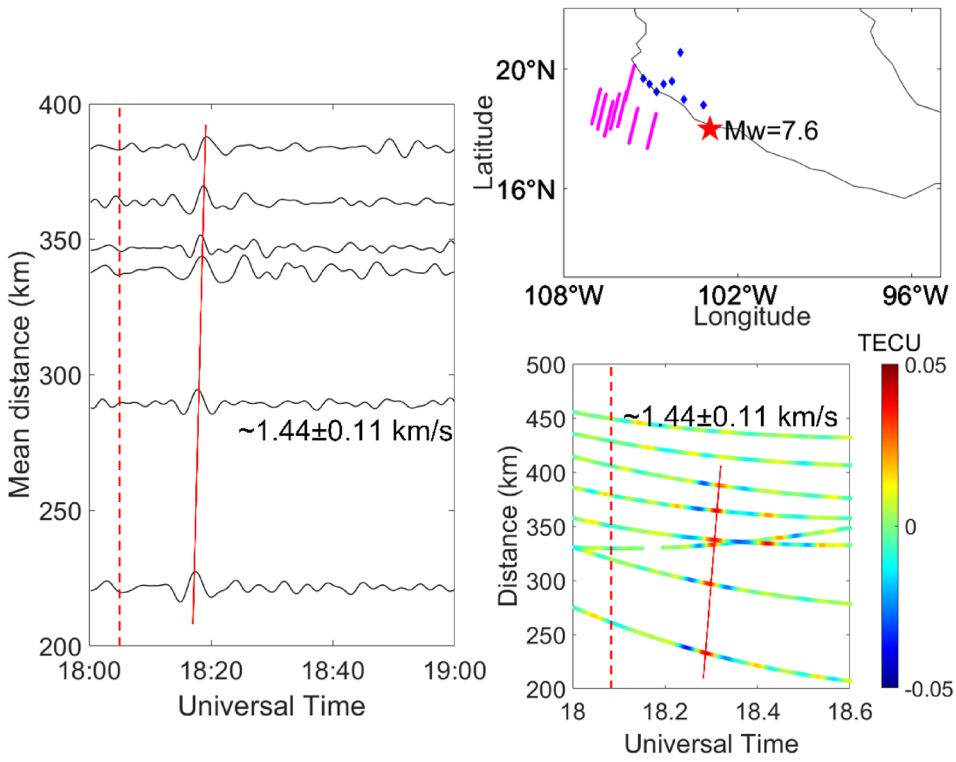

Fig. 10 CIDs from GNSS stations for G32 during 18:00–19:00 with TEC time series (left panel), SIPs track (top right panel) and the travel time diagram (bottom right panel)

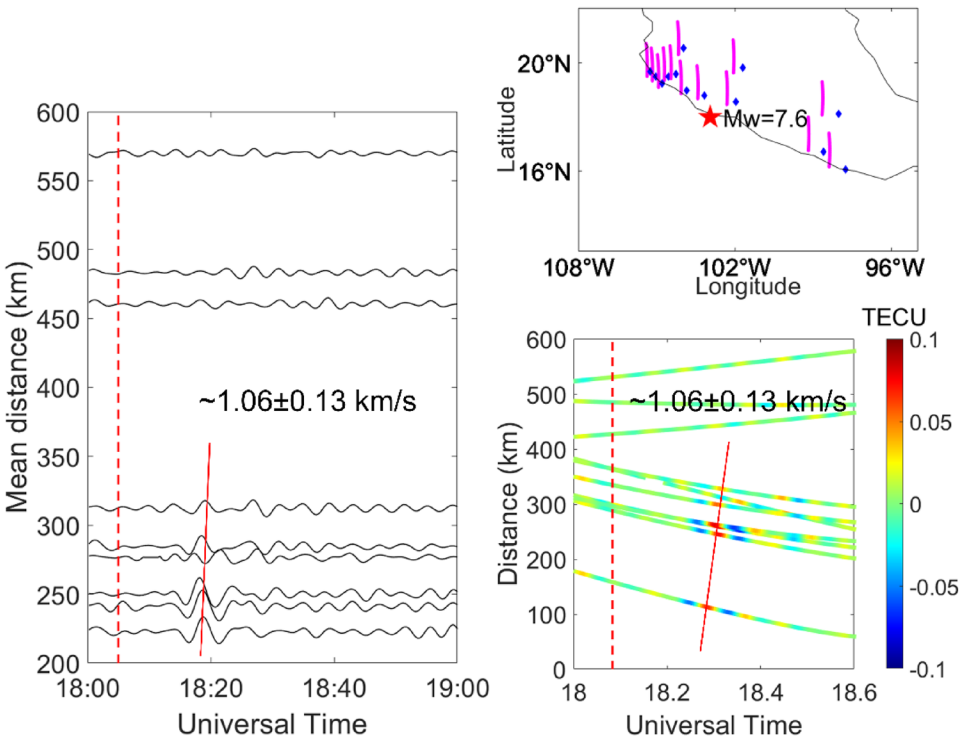

Fig. 11 CIDs from GNSS stations for R21 during 18:00–19:00 with a) the TEC time series, b) SIPs track and c) the travel time diagram

Fig. 14, while the velocity is 0–0.05 m/s in the east region. As Fig. 13 shows, most of the CIDs propagate quicker in the western region. There might be some relationships, while more studies and the data such as plate movement velocity would be helpful for the investigation and explanation in the future. In all, other factors can influence the amplitude, phase, and azimuthal asymmetry of seismic ionospheric disturbances, which should be investigated in the near future.

Summary

In this study, the CIDs following the 2022 Mexico earthquake are analyzed and investigated in details by using GNSS observation. The main results are summarized as follows:

1. Significant CIDs are observed from about 12 min to about 20 min after the Mexico earthquake in the northern region and propagate from epicenters to the far field.
2. The CID signals have a central frequency of about 2–4 mHz, which is within the range of acoustic wave frequency.
3. The CIDs are the typical *N*-shaped and inverse *N*-shaped, which are related to the vertical crustal motion, the influence of geomagnetic field, geometric factors and filtering parameters.
4. The amplitude of TEC is different, which may be caused by the observation geometry.
5. The propagation velocity is different in different azimuth directions with 0.81 km/s, 1.01 km/s, 1.16 km/s, 1.44 km/s and 1.06 km/s, respectively, which are all close to the acoustic wave velocity. The difference between the velocities might be caused by the rupture direction and geomagnetic field.

These findings demonstrate that CIDs can potentially provide details on the particular earthquake process. More case studies are required to confirm the different propagation velocities in the various azimuth directions as well as the complex process underlying earthquake-atmospheric coupling in the future.

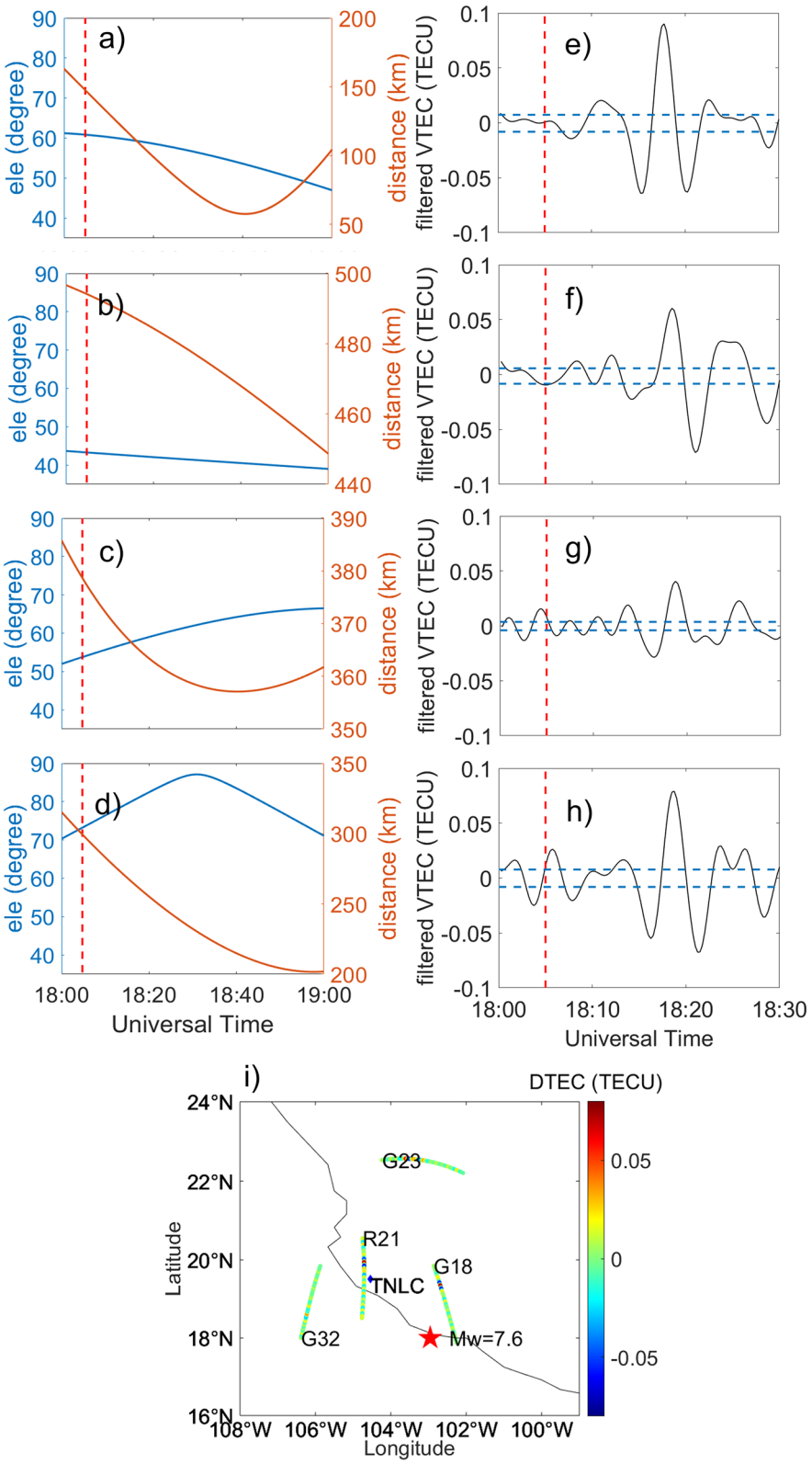

Fig. 12 TEC, elevation angle, distance and SIP track from epicenter with the combination of TNLC with different satellites. **a**, **b**, **c** and **d** are elevation angle and distance with G18, G23, G32 and R21, respectively. **e**, **f**, **g** and **h** are TEC with G18, G23, G32 and R21, respectively. i) is the SIP track of the different combination

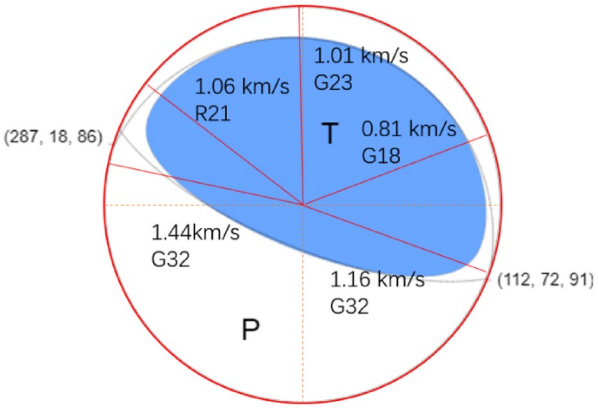

Fig. 13 CID propagation velocity and the beach ball. The beach ball is available from https://earthquake.usgs.gov/earthquakes/eventpage/us7000i9bw/moment-tensor

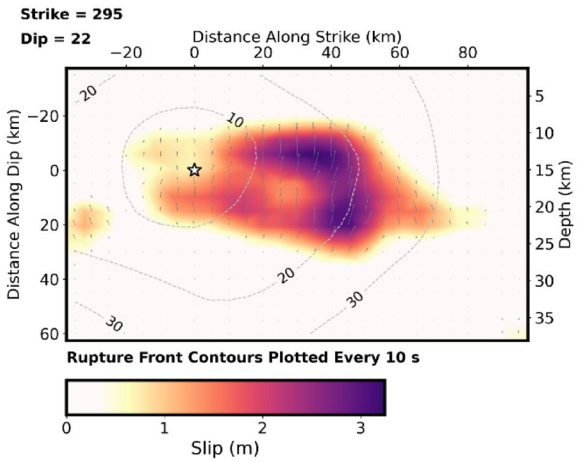

Fig. 14 Cross-section of slip distribution. The strike direction is indicated above each fault plane, and the hypocenter location is denoted by a star. Slip amplitude is shown in color and the motion direction of the hanging wall relative to the footwall (rake angle) is indicated with arrows. Contours show the rupture initiation time in seconds (https://earthquake.usgs.gov/earthquakes/eventpage/us7000i9bw/finite-fault)

Acknowledgements This study was funded by the National Natural Science Foundation of China (NSFC) Project (Grant No. 12073012).

Author contributions LL wrote the main manuscript. LL and YC provided the methodology and software. SJ supervised this article and reviewed this paper. All authors reviewed the manuscript.

Data availability The space weather index can be obtained at https://spdf.gsfc.nasa.gov/. The GNSS observation data from UNAVCO are available at https://www.unavco.org/data/. And precise orbit products are from CDDIS (https://cddis.nasa.gov/). The focal mechanism is obtained from U.S. Geological survey (https://earthquake.usgs.gov/earthquakes/eventpage/us7000i9bw/moment-tensor) and IRIS (http://ds.iris.edu/spud/momenttensor/20746202).

Declarations

Conflict of interests The authors declare no competing interests.

References

Afraimovich EL, Perevalova NP, Plotnikov AV, Uralov AM (2001) The shock-acoustic waves generated by earthquakes. Ann Geophys 19(4):395–409. https://doi.org/10.5194/angeo-19-395-2001

Artru J, Farges T, Lognonne L (2004) Acoustic waves generated from seismic surface waves: propagation properties determined from Doppler sounding observations and normal-mode modelling. Geophys J Int 158(3):1067–1077. https://doi.org/10.1111/j.1365-246X.2004.02377.x

Astafyeva E, Heki K (2009) Dependence of waveform of near-field coseismic ionospheric disturbances on focal mechanisms. Earth Planets Space 61:939–943. https://doi.org/10.1186/BF03353206

Astafyeva E, Heki K, Vladislav K, Afraimovich E, Shalimov S (2009) Two-mode long-distance propagation of coseismic ionosphere disturbances. J Geophys Res Space Phys 114(A10):A10307. https://doi.org/10.1029/2008ja013853

Astafyeva E, Shalimov S, Olshanskaya E, Lognonné P (2013) Ionospheric response to earthquakes of different magnitudes: larger quakes perturb the ionosphere stronger and longer. Geophys Res Lett 40(9):1675–1681. https://doi.org/10.1002/grl.50398

Astafyeva E, Rolland LM, Sladen A (2014a) Strike-slip earthquakes can also be detected in the ionosphere. Earth Planet Sci Lett 405:180–193. https://doi.org/10.1016/j.epsl.2014.08.024

Astafyeva E, Yasyukevich Y, Maksikov A, Zhivetiev I (2014b) Geomagnetic storms, super-storms, and their impacts on GPS-based navigation systems. Space Weather 12(7):508–525. https://doi.org/10.1002/2014sw001072

Bagiya MS, Sunil A, Rolland L, Nayak S, Ponraj M, Dhanya T, Durbha SR (2019) Mapping the impact of non-tectonic forcing mechanisms on GNSS measured coseismic ionospheric perturbations. Sci Rep 9(1):18640. https://doi.org/10.1038/s41598-019-54354-0

Bird P (2003) An updated digital model of plate boundaries. Geochem Geophys Geosyst 4(3):1027. https://doi.org/10.1029/2001GC000252

Brunini FJ, Azpilicueta FJ (2009) Accuracy assessment of the GPS-based slant total electron content. J Geodesy 83(8):773–785. https://doi.org/10.1007/s00190-008-0296-8

Cahyadi MN, Heki K (2015) Coseismic ionospheric disturbance of the large strike-slip earthquakes in North Sumatra in 2012: Mw dependence of the disturbance amplitudes. Geophys J Int 200(1):116–129. https://doi.org/10.1093/gji/ggu343

Calais E, Minster JB (1995) GPS detection of ionospheric perturbations following the January 17, 1994, Northridge earthquake. Geophys Res Lett 22:1045–1048. https://doi.org/10.1029/95GL00168

Chai Y, Jin SG (2021) Two-azimuth co-seismic ionospheric disturbances following the 2020 Jamaica earthquake from GPS observations. J Geophys Res Space Phys. https://doi.org/10.1029/2020ja028995

DeMets C, Gordon RG, Donald FA (2010) Geologically current plate motions. Geophys J Int 181(1):1–80. https://doi.org/10.1111/j.1365-246X.2009.04491.x

Ducic V, Artru J, Lognonne P (2003) Ionospheric remote sensing of the Denali earthquake Rayleigh surface waves. Geophys Res Lett 30(18):1951. https://doi.org/10.1029/2003gl017812

Gao C, Jin SG, Yuan LL (2020) Ionospheric responses to the June 2015 geomagnetic storm from ground and LEO GNSS observations. Remote Sens. https://doi.org/10.3390/rs12142200

Heise S, Jakowski N, Wehrenpfennig A, Reigber C, Lühr H (2002) Sounding of the topside ionosphere/plasmasphere based on GPS measurements from CHAMP: initial results. Geophys Res Lett 29(14):41–44. https://doi.org/10.1029/2002gl014738

Heki K, Otsuka Y, Choosakul N, Hemmakorn N, Komolmis T, Maruyama T (2006) Detection of ruptures of Andaman fault segments in the 2004 great Sumatra earthquake with coseismic ionospheric disturbances. J Geophys Res. https://doi.org/10.1029/2005jb004202

Heki K, Ping JS (2005) Directivity and apparent velocity of the coseismic ionospheric disturbances observed with a dense GPS array. Earth Planet Sci Lett 236(3–4):845–855. https://doi.org/10.1016/j.epsl.2005.06.010

Jin R, Jin SG, Feng GP (2012) M_DCB: Matlab code for estimating GNSS satellite and receiver differential code biases. GPS Solut 16:541–548. https://doi.org/10.1007/s10291-012-0279-3

Jin SG, Occhipinti G, Jin R (2015) GNSS ionospheric seismology: recent observation evidences and characteristics. Earth-Sci Rev 147:54–64. https://doi.org/10.1016/j.earscirev.2015.05.003

Jin SG, Jin R, Li D (2017) GPS detection of ionospheric Rayleigh wave and its source following the 2012 Haida Gwaii earthquake. J Geophys Res Space Phys 122(1):1360–1372. https://doi.org/10.1002/2016ja023727

Liu J, Chen C, Lin C, Tsai H, Chen C, Kamogawa M (2011) Ionospheric disturbances triggered by the 11 March 2011M9.0 Tohoku earthquake. J Geophys Res Space Phys 116(A6):A06319. https://doi.org/10.1029/2011ja016761

Liu C, Lay T, Bai Y, He P, Xiong X (2023) Coseismic slip model of the 19 September 2022 Mw 7.6 Michoacán, Mexico, Earthquake: A Quasi-repeat of the 1973 Mw 7.6 Rupture. The Seismic Record 3(2):57–68. https://doi.org/10.1785/0320220042

Mendoza C, Hartzell SH (1989) Slip distribution of the 19 September 1985 Michoacan, Mexico, earthquake: near-source and Teleseismic constraints. Bull Seismol Soc Am 79(3):655–669

Mendoza C, Hartzell S (1999) Fault-slip distribution of the 1995 Colima-Jalisco, Mexico, earthquake. Bull Seismol Soc Am 89(5):1338–1344. https://doi.org/10.1785/BSSA0890051338

Ortiz M, Singh SK, Pacheco J, Kostoglodov V (1998) Rupture length of the October 9, 1995 Colima-Jalisco earthquake (Mw8) estimated from tsunami data. Geophys Res Lett 25(15):2857–2860. https://doi.org/10.1029/98gl02059

Reyes A, Brune JN, Lomnitz C (1979) Source mechanism and aftershock study of the Colima, Mexico earthquake of January 30, 1973. Bull Seismol Soc Am 69(6):1819–1840. https://doi.org/10.1785/BSSA0690061819

Rolland LM, Lognonne P, Munekane H (2011) Detection and modeling of Rayleigh wave induced patterns in the ionosphere. J Geophys Res Space Phys. https://doi.org/10.1029/2010ja016060

Rolland LM, Vergnolle M, Nocquet J, Sladen A, Dessa J, Tavakoli F, Nankali HR, Cappa F (2013) Discriminating the tectonic and non-tectonic contributions in the ionospheric signature of the 2011, Mw7.1, dip-slip Van earthquake. Eastern Turkey. Geophys Res Lett 40(11):2518–2522. https://doi.org/10.1002/grl.50544

Santoyo MA, Mikumo T, Quintanar L (2006) Faulting process and coseismic stress change during the 30 January, 1973, Colima, Mexico interplate earthquake (Mw=7.6). Geofísica Internacional 45:163–178

Singh SK, Ponce L, Nishenko SP (1985) The great Jalisco, Mexico, earthquakes of 1932: subduction of the Rivera plate. Bull Seismol Soc Am 75(5):1301–1313. https://doi.org/10.1785/BSSA0750051301

Tsugawa T, Saito A, Otsuka Y, Nishioka M, Maruyama T, Kato H, Murata KT (2011) Ionospheric disturbances detected by GPS total electron content observation after the 2011 off the Pacific coast of Tohoku Earthquake. Earth, Planets and Space 63(7):875–879. https://doi.org/10.5047/eps.2011.06.035

Yagi Y, Mikumo T, Pacheco J, Reyes G (2004) Source Rupture Process of the Tecomán, Colima, Mexico Earthquake of 22 January 2003, Determined by Joint Inversion of Teleseismic Body-Wave and Near-Source Data. Bull Seismol Soc Am 94(5):1795–1807. https://doi.org/10.1785/012003095

Zakharov VI, Gorchakov GI (2017) GPS observation of traveling ionospheric disturbances related to Moscow megacity. Adv Space Res 59(2):614–618. https://doi.org/10.1016/j.asr.2016.11.001

Linlin Li is a Ph.D student at Shanghai Astronomical Observatory, Chinese Academy of Sciences, Shanghai, China. Her current research mainly focuses on Space Science, Ionospheric Modelling, Satellite Navigation and Remote Sensing.

Shuanggen Jin is a Professor at Shanghai Astronomical Observatory, CAS, Shanghai, China and Vice-President of Henan Polytechnic University, Jiaozuo, China, Member of Academia Europaea. He received a Ph.D. from the University of Chinese Academy of Sciences in 2003 and a B.Sc from Wuhan University in 1999. He has been on Space Geodesy, Satellite Navigation and Remote Sensing.

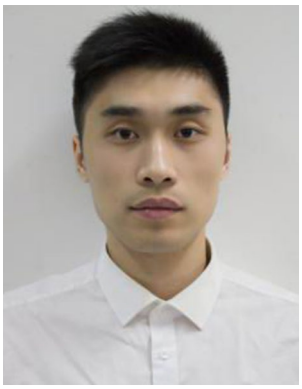

Yi Chai is a Ph.D student at Shanghai Astronomical Observatory, Chinese Academy of Sciences, Shanghai, China. His current research mainly focuses on Space Geodesy and Planetary Science.